

THERMAL EFFECTS ON THE STRUCTURAL AND MECHANICAL MICROSTRUCTURE PARAMETERS OF SILICEOUS SANDSTONE FROM KIELCE UPLAND

Michał PACHNICZ¹

Department of Geotechnics, Hydrotechnics, Underground and Hydraulic Engineering, Faculty of Civil Engineering, Wrocław University of Science and Technology, Wrocław, Poland

Abstract

This study explores the thermal evolution of the microstructure and mechanical properties of Jurassic sandstone from the Kielce Upland, subjected to temperatures between 20°C and 1000°C. Combining microcomputed tomography (micro-CT) and nanoindentation techniques, it analyzes how geometric changes affect mechanical parameters. Key features like porosity, pore size distribution, and solid matrix thickness were assessed alongside indentation modulus (M_{IT}) and hardness (H_{IT}). The results reveal a strong correlation between microstructural changes and mechanical responses. At 200°C, microstructural compaction and thermal tightening lead to temporary strengthening. Above 600°C, increased porosity, microcrack formation, and rock matrix degradation cause significant reductions in mechanical properties. Reconstructed grayscale values are identified as reliable estimators for mechanical property changes, particularly for indentation modulus, when baseline parameters are available.

Keywords: sandstone, tomography, nanoindentation, temperature, microstructure

1. INTRODUCTION

The behavior of rocks under high-temperature conditions is a critical factor in the design and optimization of energy storage systems, radioactive waste repositories, and tunneling projects [1],[2]. Moreover, understanding the changes occurring in rock materials during thermal exposure is essential for improving the efficiency of geothermal resource extraction and the recovery of fossil fuels [3]. Over the past decades, numerous studies have established a strong correlation between temperature and the physical, mechanical, and thermal properties of rocks. Research has consistently shown that high-temperature exposure leads to a reduction in macroscopic mechanical parameters, as observed across a

¹ Corresponding author: Michał Pachnicz, Wrocław University of Science and Technology, Faculty of Civil Engineering, Department of Geotechnics, Hydrotechnics, Underground and Hydraulic Engineering, Grunwaldzki Square 11, 50-377 Wrocław, michal.pachnicz@pwr.edu.pl, +48 713204354

range of rock types, including granite, sandstone, and shale [4]–[7]. These macroscopic property changes are widely attributed to microstructural transformations within the rock material (Fig. 1).

Understanding the behavior of rocks under high-temperature conditions is essential for designing energy storage facilities, radioactive waste repositories, and tunnel systems. Additionally, studying the changes in rock materials subjected to high temperatures is critical for optimizing the extraction of geothermal resources and various fossil fuels. Over recent decades, research on the effects of temperature on rock properties has provided substantial evidence of a strong relationship between temperature and the physical, mechanical, and thermal properties of rocks. Numerous studies have shown a clear correlation between the decrease in macroscopic mechanical parameters and high-temperature exposure in various rock types, including granite, sandstone, and shale. It is widely recognized that changes in macroscopic rock properties, particularly mechanical properties, are a result of microstructural changes within the rock material.

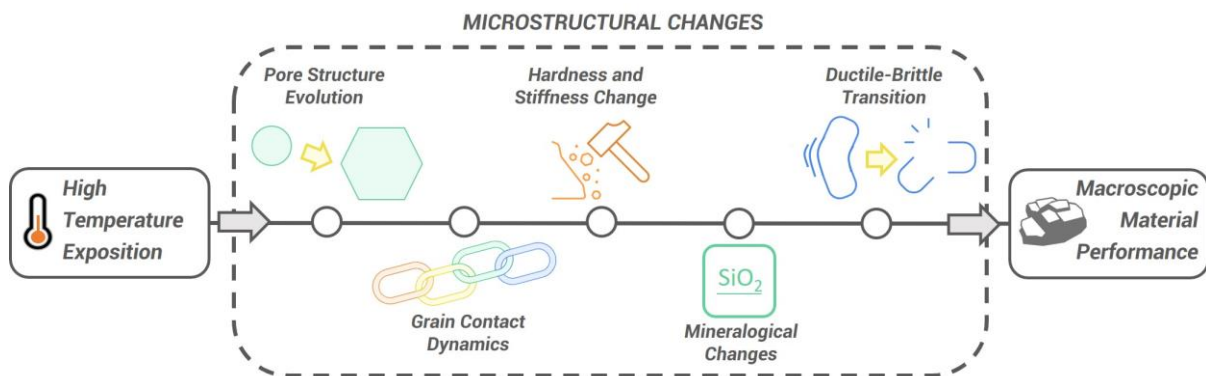


Fig. 1. Microstructural changes occurring in the structure of rock material. Initially, smaller pores may coalesce into larger ones due to thermal expansion and grain rearrangement. Additionally, the evolution of the pore structure directly influences permeability. At lower temperatures, grains may be loosely packed with significant pore space, but as temperature rises, grains can become more tightly bonded due to sintering effects. This densification typically enhances mechanical strength and stiffness up to a certain temperature threshold (around 600°C) before leading to brittleness at higher temperatures. What is more, certain minerals may dehydrate or undergo phase transitions [8]–[12]

Despite significant progress, the relationship between microstructural evolution and the mechanical behavior of sandstone under high-temperature conditions remains poorly understood. Existing studies typically focus on either strength parameter evolution or microstructural morphology, with few efforts to integrate these aspects [9],[13]–[15]. Microstructural observations are often interpreted in relation to macroscopic properties, such as compressive strength [10],[16], rather than directly linked to microscale mechanical parameters.

To address this gap, the present study investigates the evolution of the microstructure and mechanical properties of siliceous sandstone subjected to temperatures ranging from 20°C to 1000°C. X-ray microcomputed tomography (micro-CT) was employed to analyze geometric changes in the microstructure [17]–[21], while the nanoindentation technique was used to evaluate mechanical properties at the microscale [22]–[26]. Both methods have demonstrated their effectiveness in characterizing various rock types [27]–[33]. The samples tested in this study represent the first in a series of investigations aimed at systematically characterizing microstructural changes in different types of sandstones under high-temperature exposure (Fig. 2a).

2. MATERIALS AND METHODS

2.1. Materials used

Sandstone from Kielce Upland was selected for this stage of research as it is almost a model example of siliceous sandstone. The Jurassic sandstones in the Kielce Upland (Fig. 2b) were primarily deposited in coastal shelf environments, which were periodically lagoonal, within an Early Jurassic brackish basin characterized by low-salinity marine conditions. This depositional setting facilitated the formation of quartz-rich sandstones [34]. They are predominantly fine-grained and exhibit siliceous or siliceous-clayey cementation. These sandstones are typically light-colored, ranging from white to yellow hues. Based on its observed composition and texture, the sandstone can be preliminarily classified as a fine-grained feldspathic arenite according to Folk's classification [35]. However, detailed petrographic analysis is recommended to confirm its mineralogical composition and validate this classification. In addition, historically, the Jurassic sandstones of the Kielce Upland have been extensively quarried and utilized in architecture and engineering projects.

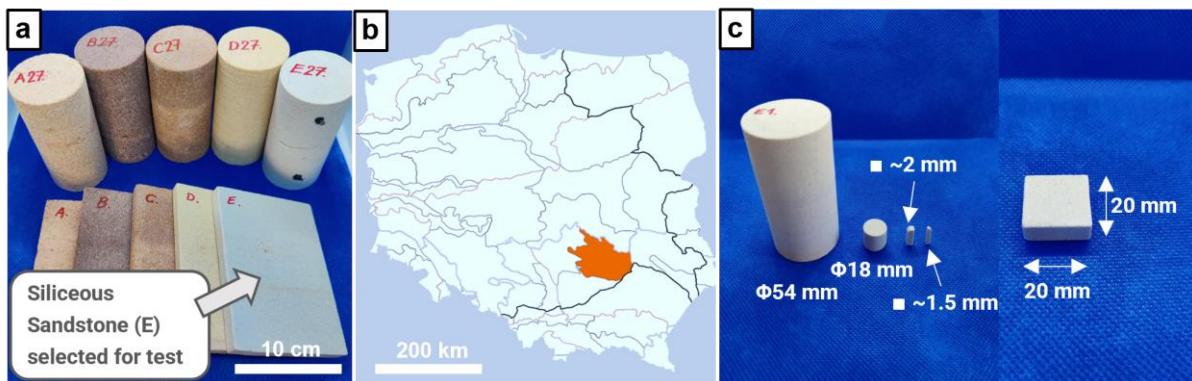


Fig. 2. Sandstone samples with the series selected for the presented study (a), geological region where the studied sandstone was sourced (Kielce Upland)- orange color (b), samples of rock material trimmed down to their final size (c)

2.2. Experimental Setup

Samples were extracted from larger blocks of sandstone using diamond core drill bits and a precision circular saw (Pace Technologies MEGA-M250). For micro-CT imaging, the samples were prepared as prisms measuring approximately $2 \times 2 \times 10$ mm, while for nanoindentation, the sample dimensions were approximately $20 \times 20 \times 5$ mm (Fig. 2c). A total of five samples (EX1–EX5) were designated for microcomputed tomography (micro-CT) analysis, and six samples (E0–E5) were designated for nanoindentation testing. Prior to experimentation, all sandstone samples were dried in a desiccator for 48 hours to remove residual moisture and standardize material properties.

Reference Micro-CT Scanning: Micro-CT imaging was conducted on samples EX1–EX5 to establish baseline geometries prior to thermal exposure. Scans were performed using a GE Phoenix v|tome|x s system with a 180 kV NanoFocus tube. Imaging was carried out in the air-dried state with a resolution of $4 \mu\text{m}$. The scanning parameters included a voltage of 60 kV, a current of $150 \mu\text{A}$, and an exposure time of 500 ms, with six averaged frames per projection. A total of 1500 projections (Fig. 3a) were acquired per sample. The projections were reconstructed into 3D digital grayscale models (Fig. 3b) using the Feldkamp algorithm in Phoenix Datasx 2 rec software. These models were analyzed to extract microstructural metrics, including grayscale distribution (Fig. 3c) and volume changes. The

grayscale values correspond to the reconstructed radiation absorption coefficient γ_{rec} , representing local density as determined by the Lambert-Beer Law of radiation attenuation [36]–[38].

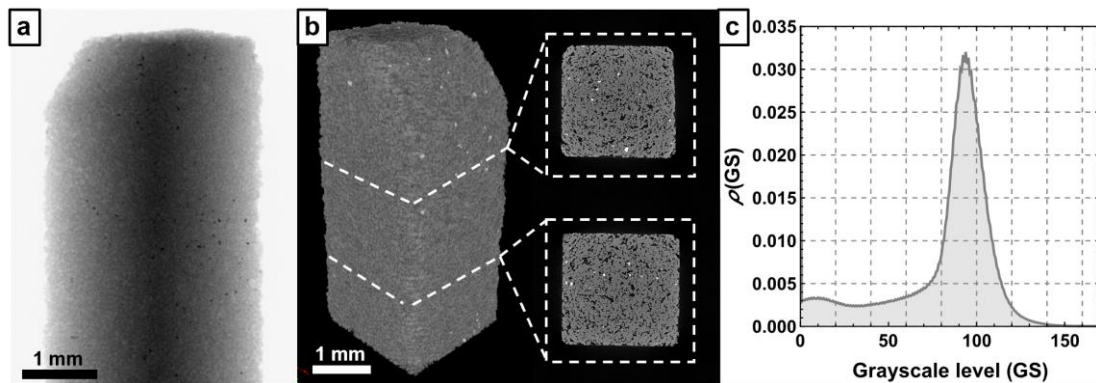


Fig. 3. A single projection for sample EX1 (a)- the brightness at each point of the image depends on the total amount of radiation absorbed by the scanned sample; reconstructed 3D digital grayscale image of the sample built from stack of 2D slices (b); PDF distribution of the reconstructed radiation absorption coefficient (grayscale) for sample EX2 (c)

To quantify the evolution of pore space and the solid matrix, binarized microstructure images were analyzed within defined volumes of interest (VOIs) (Fig. 4). The binarization threshold was determined using Otsu’s method [39], while the VOI was dynamically defined using the ROI-Shrink-Wrap function [40], which iteratively adjusts the region of interest for each slice of the reconstructed geometry.

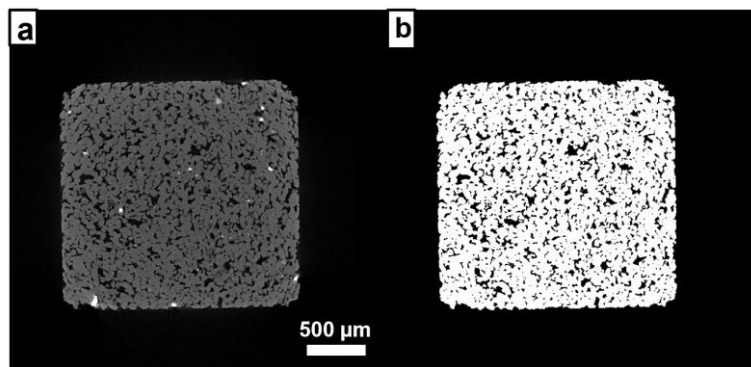


Fig. 4. Thresholded section of sample EX4: grayscale image (a), binarized image within the ROI (b)

Thermal Treatment: Thermal exposure was carried out in a Neoterm MidiSUN laboratory furnace, following a controlled heating program with specific temperature thresholds (Fig. 4). Six temperatures were investigated: 20°C (EX1–EX5 as reference scans, E0), 200°C (EX5, E5), 400°C (EX4, E4), 600°C (EX3, E3), 800°C (EX2, E2), and 1000°C (EX1, E1). This sequential heating protocol allowed for a systematic evaluation of thermal effects on the sandstone.

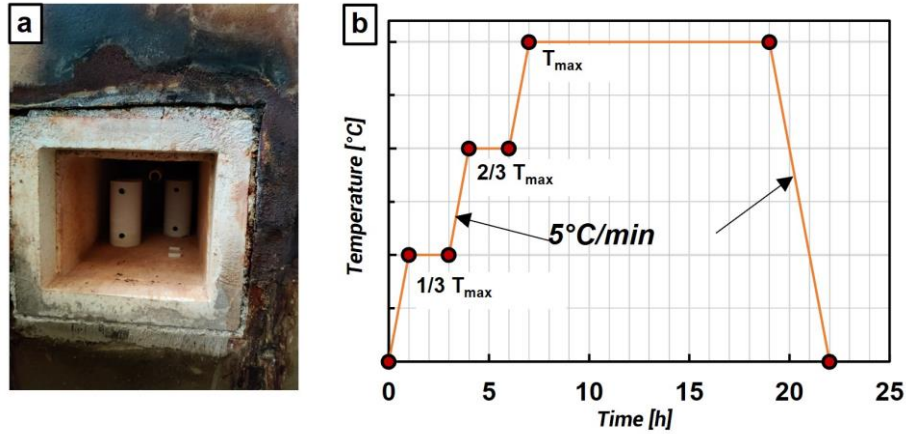


Fig. 5. Neotherm Midi SUN furnace chamber with samples placed inside (a), temperature increase, and furnace cooling function applied for the study (b)

Post-Treatment Micro-CT Scanning: After temperature exposure, the EX1 to EX5 samples were once again scanned using micro-CT using the same resolution and lamp settings as for reference scans. This allowed for capturing the evolution of microstructural geometry and identification of morphological changes induced by thermal stress.

Surface Preparation for Nanoindentation: Thermally treated samples (E0–E5) were embedded in low-viscosity epoxy resin using a cold-mounting process to stabilize them for mechanical testing. Embedding was conducted in a Struers CitoVac vacuum chamber. After embedding, samples were subjected to sequential grinding and polishing to achieve the surface quality required for reliable nanoindentation. Preparation steps included initial flattening with SiC polishing pads, fine grinding with MD-Piano diamond-coated discs (up to MD-Piano 2000), and final polishing with MD-Piano 4000 and MD-Chem using OP-S NonDry 0.004 μm colloidal silica suspension. After each step, samples were cleaned in an ultrasonic bath with 99% isopropanol for 30 seconds

Micromechanical Testing: Nanoindentation tests were performed on samples E0–E5 using a CSM Instruments NHT2 nanoindenter equipped with a Berkovich diamond tip. A Grid Indentation Technique [41]–[43] was used, involving 3600 indentations spaced 30 μm apart. Each indentation was load-controlled to a maximum depth of $h_{\text{max}}=1\ \mu\text{m}$, approximately 25% of the micro-CT resolution. The basic microstructural mechanical characteristics, namely indentation modulus M_{IT} (2.1) and hardness H_{IT} (2.2) [44],[45] were calculated using the following equations:

$$M_{\text{IT}} = \frac{1}{2\beta} S \frac{\sqrt{\pi}}{\sqrt{A}} \quad [\text{GPa}], \quad (2.1)$$

$$H_{\text{IT}} = \frac{P_{\text{max}}}{A} \quad [\text{GPa}], \quad (2.2)$$

where A is the projected contact area at the maximum load P_{max} estimated from the equation $A=F(h)$ [46], S is the contact stiffness (N/m), which is the slope of the unloading curve at maximum indentation depth h_{max} and β is the correction factor for the geometry of the indenter (for Berkovich tips, $\beta \approx 1.034$) [47].

The indentation modulus (M_{IT}) represents the elastic response of a material to localized stress under the indenter, derived from the contact stiffness, projected contact area, and indenter geometry. For isotropic, homogeneous materials, it is related to Young's modulus (E) by the equation (2.3):

$$M_{IT} = \frac{E}{1-\nu^2} \quad [GPa], \quad (2.3)$$

where E is the Young's modulus and ν is the Poisson's ratio of the tested material. This relationship assumes the indenter's material has a significantly higher modulus (e.g., diamond), than the modulus of the tested material. In heterogeneous materials like sandstone, M_{IT} reflects the combined elastic behaviour of grains and the matrix, making it a key parameter for evaluating local stiffness.

Hardness (H_{IT}), measured as the ratio of maximum load (P_{max}) to the projected contact area (A), is an indicator of a material's resistance to localized plastic deformation. For many materials, hardness can be used as a proxy for estimating uniaxial compressive strength (UCS) or other macroscopic strength parameters. The relationship between hardness and strength depends on the material type and is typically empirically established [48]–[51]

Mapping of mechanical parameters covered approximately 2 mm² for each sample (Fig. 6). Statistical analyses of the nanoindentation results were conducted following established methodologies [52]–[54],[16].

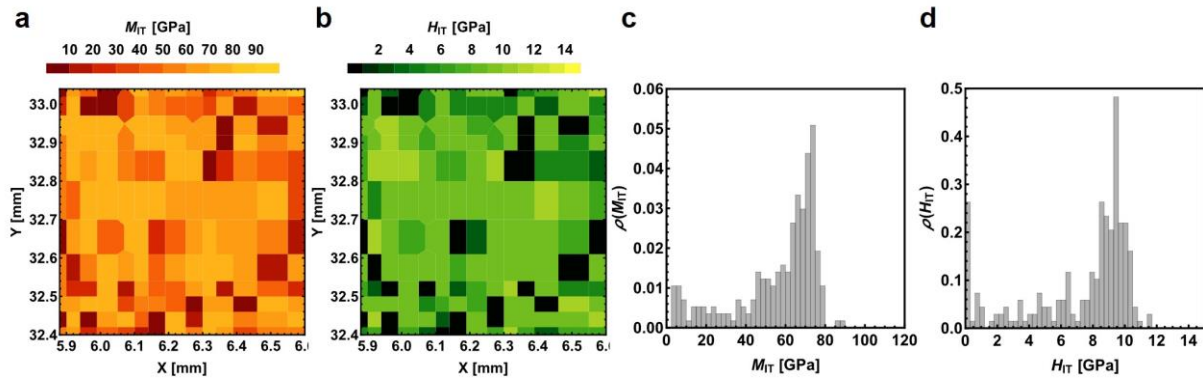


Fig. 6. Exemplary Distribution of M_{IT} (a) and H_{IT} (b) over the sample surface alongside their respective histograms (c, d)

3. RESULTS AND DISCUSSION

This section presents the results of both microcomputed tomography (micro-CT) and nanoindentation analyses. Data processing and summary of the measured values were performed using dedicated image analysis software, including Bruker CTAn, Bruker CTvox, and Bruker DataViewer, as well as custom scripts developed in Wolfram Mathematica [55]. Additionally, selected datasets were processed using modified Python 3.10 scripts [56], available in open-source repositories [57],[58].

To ensure consistency and clarity in presenting the results, a unified color scheme was adopted for samples corresponding to each temperature threshold: ■ for 20°C, ■ for 200°C, ■ for 400°C, ■ for 600°C, ■ for 800°C and ■ for 1000°C. This approach facilitates direct comparisons across temperature thresholds and provides a clear visual representation of the effects of thermal exposure on the sandstone's microstructural and mechanical properties.

To further clarify the result analysis, the basic properties of the sandstone's microstructure and mechanical parameters before thermal exposure are summarized in Table 1. These include porosity and mean values of grayscale (μGS), pore size (μP_{SITh}), solid matrix thickness (μS_{SITh}), indentation modulus (μM_{IT}), and hardness (μH_{IT}). These baseline values serve as a reference for assessing changes induced

by thermal treatment and provide a foundation for correlating microstructural evolution with mechanical performance.

Table 1. Microstructural properties of the tested sandstone before temperature exposure

Property	Value	Unit	Description
Porosity (ϕ)	17.33	%	Proportion of void space within the material.
Mean grayscale (μGS)	76.9478	-	Represents the reconstructed radiation absorption coefficient.
Mean pore size (μP_{StTh})	29.23	μm	Average diameter of pores within the microstructure.
Mean solid matrix thickness (μS_{StTh})	81.52	μm	Average thickness of solid components in the microstructure.
Mean indentation modulus (μM_{IT})	56.65	GPa	Measure of elastic response under localized stress.
Mean hardness (μH_{IT})	7.70	GPa	Material's resistance to localized plastic deformation.

3.1. Geometric morphology evolution (Micro CT results)

To evaluate the changes in morphology before and after thermal exposure, the spatial alignment of reconstructed micro-CT images was corrected using 3D registration. This process aligns the geometry of the heated samples with the reference samples within the same Cartesian coordinate system. The reconstructed microstructures for the tested samples, along with their grayscale distributions before and after thermal treatment, are presented below. Grayscale values were calculated within a defined volume of interest (VOI).

Changes in the grayscale distribution reflect alterations in the microstructure of the sandstone, corresponding to variations in the local volumetric density or material packing within the analyzed volume. Specifically:

- **Peak Shift to the Left:** Observed in the higher range of the grayscale distribution, this shift indicates the development of microcracks within the material. These microcracks may not manifest as detectable porosity at the resolution of the scan but influence the material's effective absorption of X-rays, leading to a reduction in local density.
- **Peak Shift to the Right:** This suggests the closure or healing of microcracks, often occurring at grain-to-grain contacts or at the interfaces between grains and the cementing material.

For grayscale values in the lower range, variations in the probability density function correspond to changes in the volume of "detectable" pore space, representing porosity resolvable at the given scan resolution. These observations are further illustrated in Fig. 7f. An initial increase in the mean grayscale value up to 200°C suggests densification or compaction within the sandstone, likely due to micropore reduction or improved grain-to-grain contact. However, beyond 200°C, a decline in the mean grayscale value indicates the increasing influence of microcrack formation and other structural disruptions, which reduce the material's ability to absorb X-rays effectively.

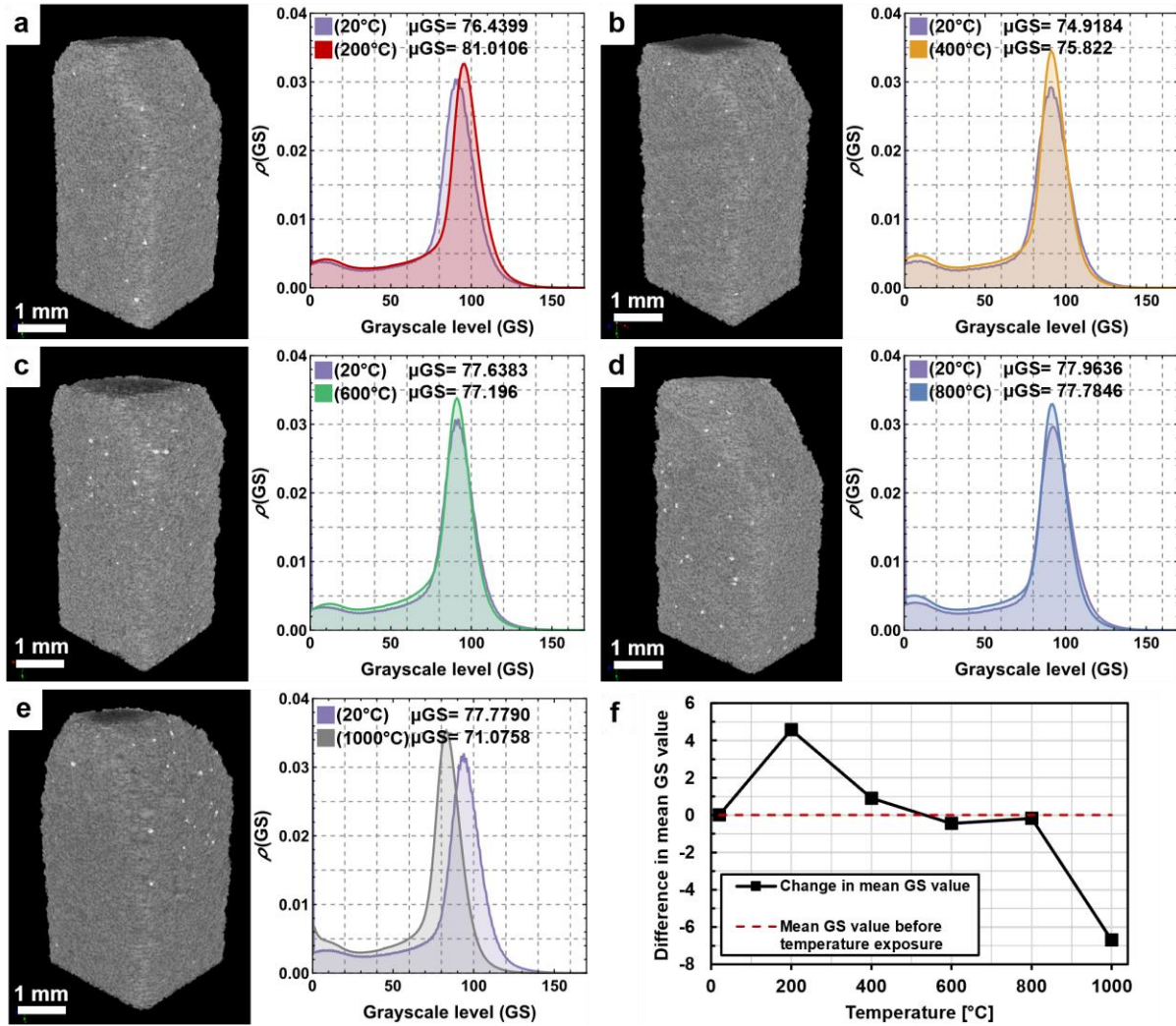


Fig. 7. Statistical analysis of the reconstructed sandstone images: digital reconstructions of the microstructure of heat-treated sandstone samples alongside their grayscale distributions - compared to the reference samples (a-e), a graph illustrating the change in mean grayscale value as a function of temperature for the tested samples (f)

The 3D volume measurements were performed using the Marching Cubes Algorithm (MCA) [40] within the defined VOI. Relative volume changes were calculated with respect to the reference volume of each sample prior to heat treatment. For temperatures ranging from 200°C to 800°C, volume changes were negligible, varying between -0.16% and 0.38%. However, at 1000°C, a significant volume increase of 20.08% was observed, which is notably higher than the typical values for sandstone, usually closer to 4% after high-temperature exposure [59].

Porosity, defined as the ratio of the total pore volume (open and closed) to the total VOI volume, was also measured using MCA. Between 200°C and 800°C, a reduction in porosity of -1.45% to -0.8% was recorded. At 1000°C, however, porosity increased by 1.27% (Fig. 8).

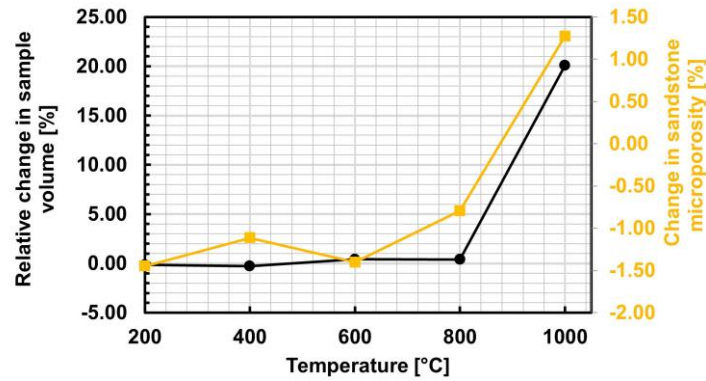


Fig. 8. Change in volume and porosity of sandstone as a function of temperature

In addition to total porosity, an advanced analysis of pore space structure was conducted, focusing on the size distribution of identified pores. A parallel analysis was performed for the solid matrix, capturing local variations in grain and cementing material volumes (Fig. 9). Both the solid matrix and pore space were characterized using the local structure thickness (St.Th.), defined as the largest radius r of a sphere fully contained within the considered phase Ω at a given point x within that phase. This relationship is expressed in Equation (3.1):

$$\tau(\vec{p}) = 2 \max(\{r | \vec{p} \in sph(\vec{x}, r) \subseteq \Omega, \vec{x} \in \Omega\}), \quad (3.1)$$

Changes in pore space and solid matrix structure confirm a distinct mechanism of microstructural evolution in sandstone, involving an initial "swelling" of the skeleton. This swelling results in a slight reduction in pore sizes, particularly at lower St.Th. values. For example, at 200°C, the percentage of pores smaller than 24 μm increases from 45.68% to 46.33%.

In contrast, at higher temperatures, a consistent trend of pore enlargement is observed, especially for pores larger than 40.1 μm , as evidenced by an increase in histogram bar heights for heat-treated samples compared to untreated ones. Additionally, all samples exhibit a systematic increase in the size of individual grains within the solid skeleton, suggesting a linear relationship between temperature and the volume expansion of the rock skeleton. This grain enlargement is particularly pronounced at 1000°C, where a significant increase in the proportion of larger grains is observed in the microstructure.

The analysis of local microstructural metrics aligns with bulk volume change observations, with the most pronounced changes occurring in the higher temperature range. These findings highlight the interplay between pore space evolution and solid matrix restructuring in driving the thermal response of sandstone.

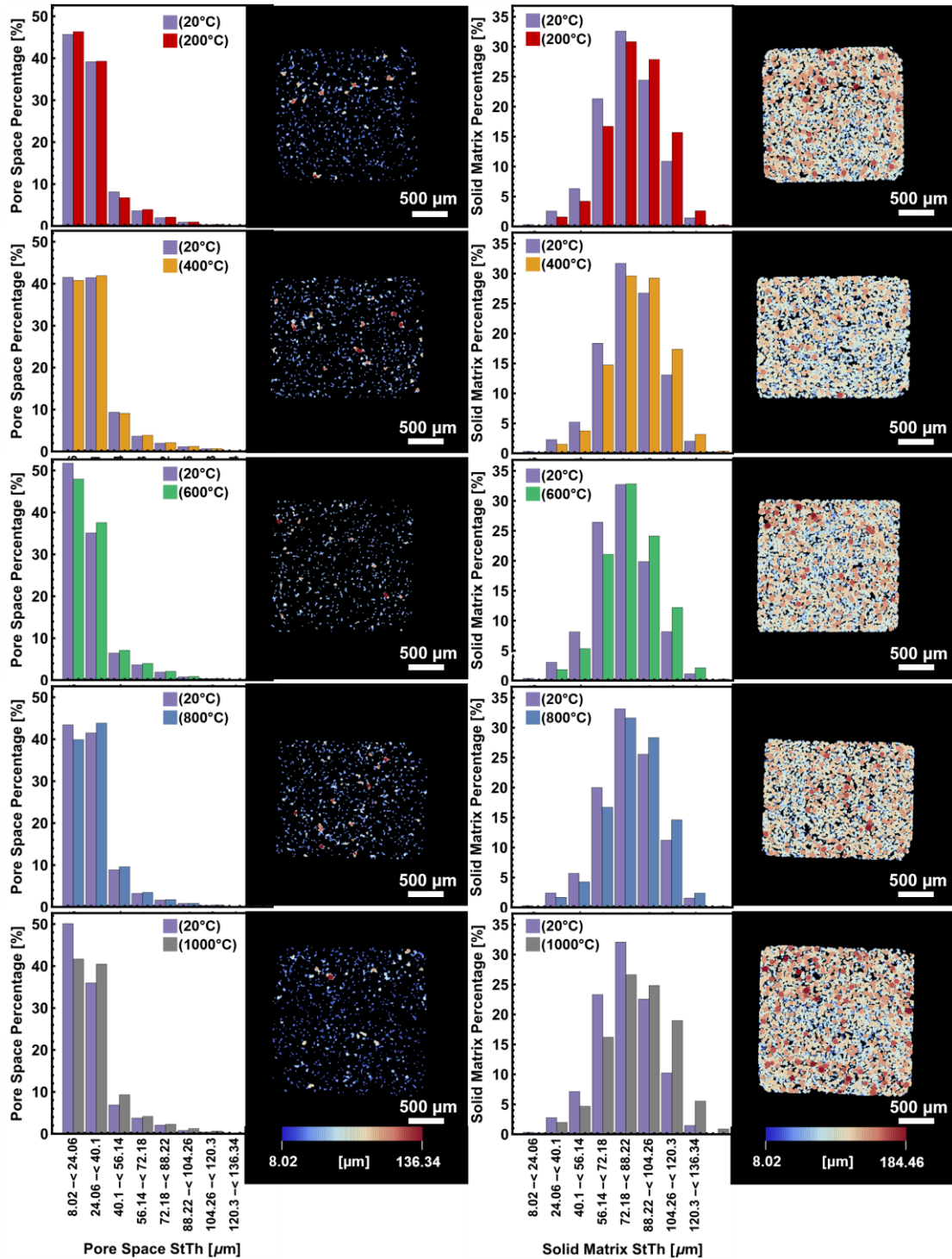


Fig. 9. Distributions of Local Structure Thickness (StTh) for pore space (left side) and solid matrix (right side) for samples EX1 – EX5. Next to the calculated distributions exemplary images of Local Structure Thickness distribution within selected slices of each sample are presented

3.2. Evolution of mechanical properties (Nanoindentation results)

An optical microscope image of the tested surface of sample E0, taken after conducting 3600 grid indentation tests (GIT), is presented in Fig. 10. The results from nanoindentation tests are displayed as distribution maps of mechanical parameters across the tested surface and histograms representing the indentation modulus (M_{IT}) and hardness (H_{IT}) metrics (Fig. 11–Fig. 16). Mean values (μ) and standard deviations (σ) for M_{IT} and H_{IT} are also reported.

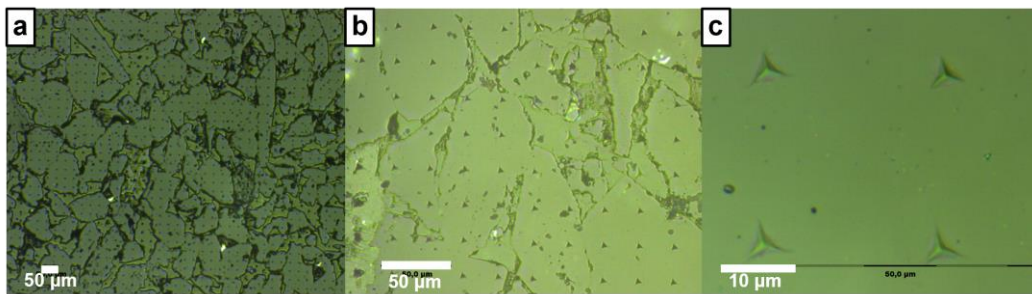


Fig. 10. Optical microscope image of the tested surface: magnification x20 (a), magnification x50 (b), magnification x200 (c)

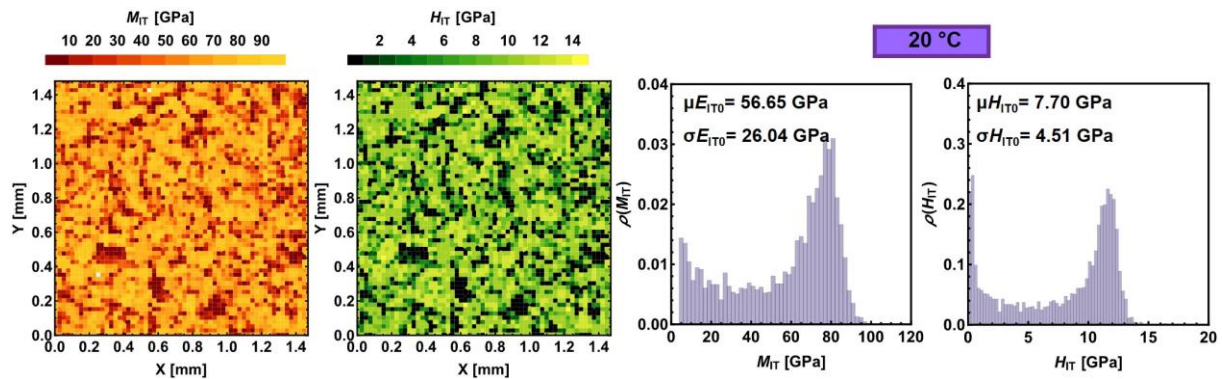


Fig. 11. Distribution maps of indentation modulus (M_{IT}) and hardness (H_{IT}) obtained from nanoindentation testing on the surface of the sandstone sample at 20°C, alongside their respective histograms

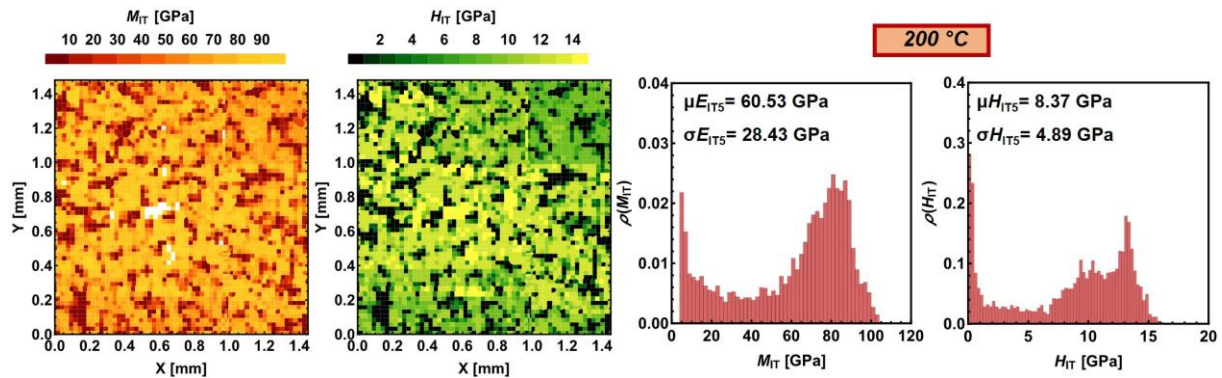


Fig. 12. Distribution maps of indentation modulus (M_{IT}) and hardness (H_{IT}) obtained from nanoindentation testing on the surface of the sandstone sample heated up to 200°C, alongside their respective histograms

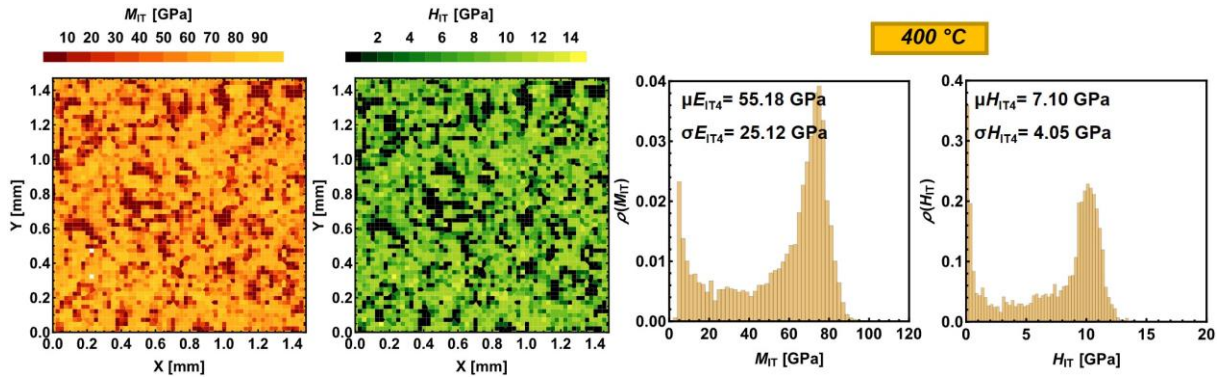


Fig. 13. Distribution maps of indentation modulus (M_{IT}) and hardness (H_{IT}) obtained from nanoindentation testing on the surface of the sandstone sample heated up to 400°C, alongside their respective histograms

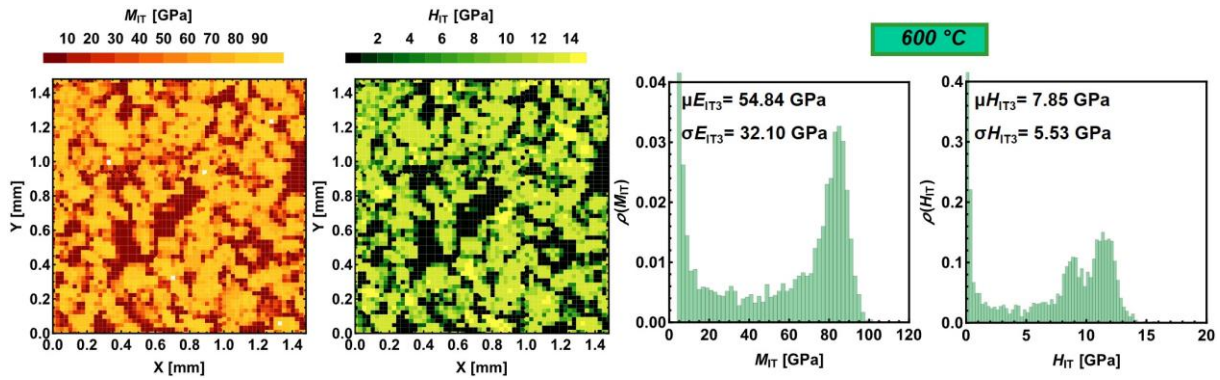


Fig. 14. Distribution maps of indentation modulus (M_{IT}) and hardness (H_{IT}) obtained from nanoindentation testing on the surface of the sandstone sample heated up to 600°C, alongside their respective histograms

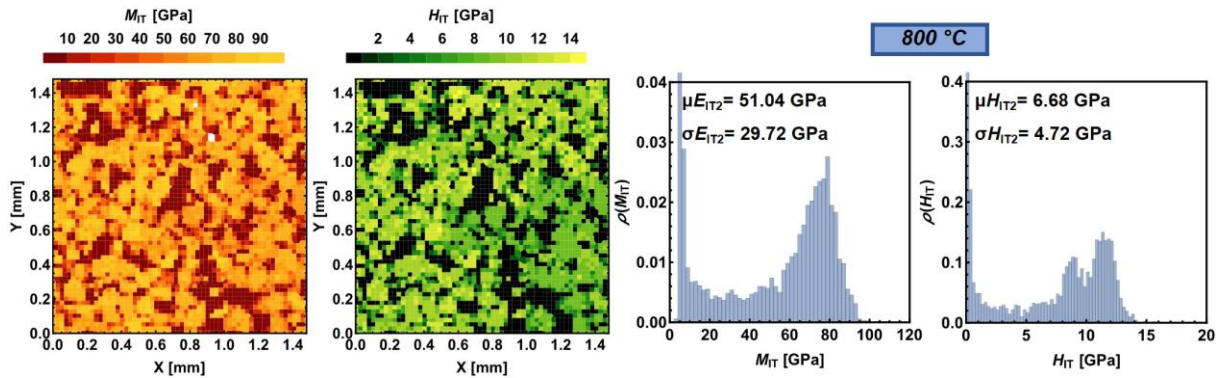


Fig. 15. Distribution maps of indentation modulus (M_{IT}) and hardness (H_{IT}) obtained from nanoindentation testing on the surface of the sandstone sample heated up to 800°C, alongside their respective histograms

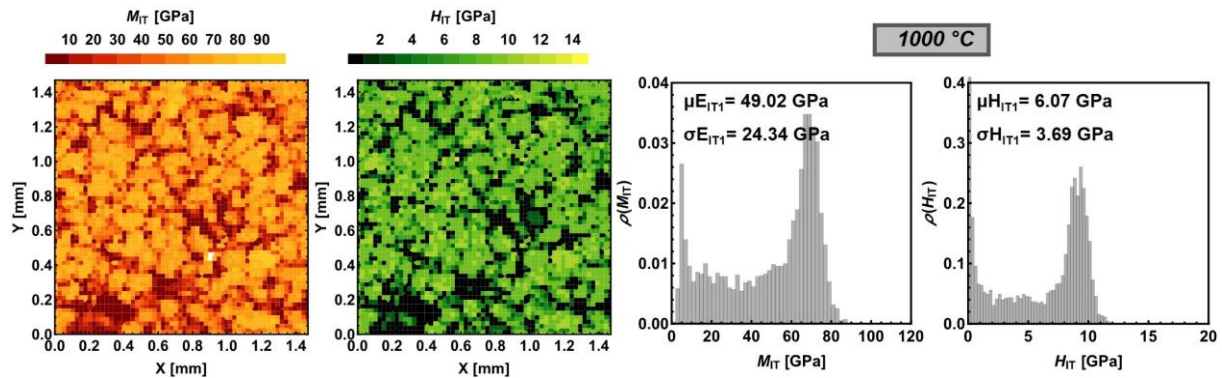


Fig. 16. Distribution maps of indentation modulus (M_{IT}) and hardness (H_{IT}) obtained from nanoindentation testing on the surface of the sandstone sample heated up to 1000°C, alongside their respective histograms

The temperature-dependent variation in the average values of indentation modulus and hardness is shown in (Fig. 17). Both parameters exhibit a general decline with increasing temperature, decreasing from 7.70 GPa to 6.07 GPa for hardness and from 56.65 GPa to 49.02 GPa for modulus. However, at 200°C, an increase in both properties is observed, with hardness rising by 0.67 GPa and modulus increasing by 3.87 GPa, corresponding to an 8.8% and 6.8% increase, respectively. This behavior suggests a strengthening effect, likely due to microstructural consolidation or thermal tightening. At 600°C (sample E3), a notable strengthening effect is observed for hardness, deviating from the trend seen in other samples. This strengthening is not as pronounced for modulus, which follows the established temperature-dependent trend.

The mean value alone does not provide sufficient insight into the mechanisms driving microstructural strengthening or weakening. To gain deeper insights, the cumulative histograms of mechanical parameter distributions were deconvoluted into the contributions of individual phases. This phase-specific decomposition was performed using a two-dimensional Gaussian Mixture Model (GMM) with $j=5$ components (A–E), selected based on the Bayesian Information Criterion [60] and Akaike Information Criterion [61]. For each component, the mean and standard deviation of M_{IT} and H_{IT} were calculated, along with their respective volume fractions (Φ_j) (Fig. 18-Fig. 23). This approach enables a detailed characterization of the mechanical properties of individual phases, providing a clearer understanding of the thermal effects on the sandstone's microstructure.

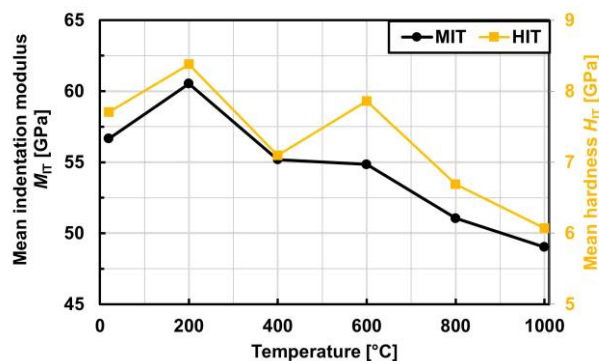


Fig. 17. Change of mean indentation modulus (M_{IT}) and mean hardness (H_{IT}) of sandstone as a function of exposure temperature

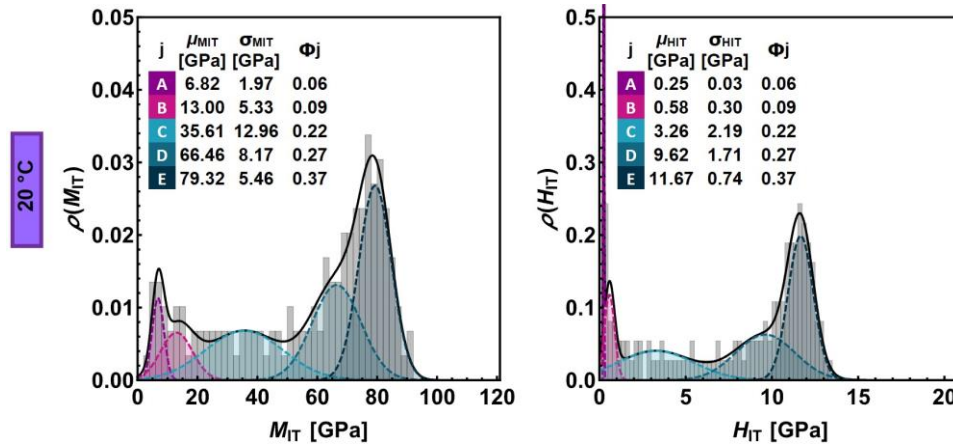


Fig. 18. Deconvoluted distributions of indentation modulus (M_{IT}) and hardness (H_{IT}) at 20°C, with Gaussian mixture components (A to E) identified

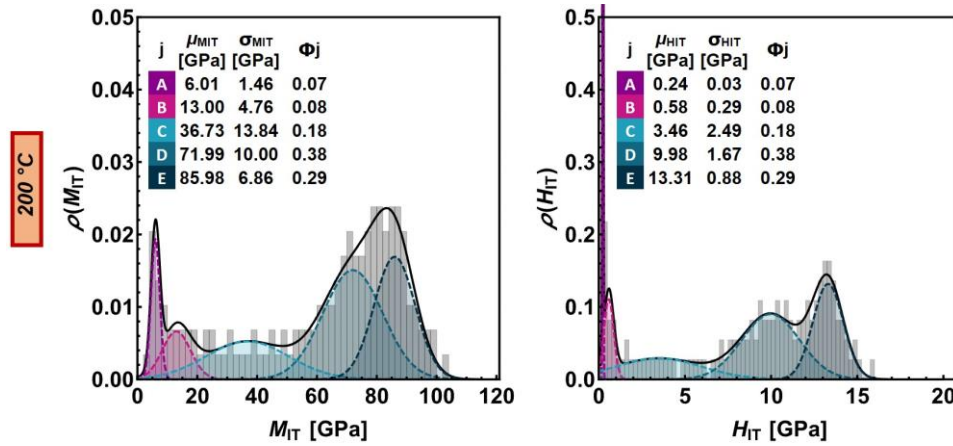


Fig. 19. Deconvoluted distributions of indentation modulus (M_{IT}) and hardness (H_{IT}) at 200°C, with Gaussian mixture components (A to E) identified

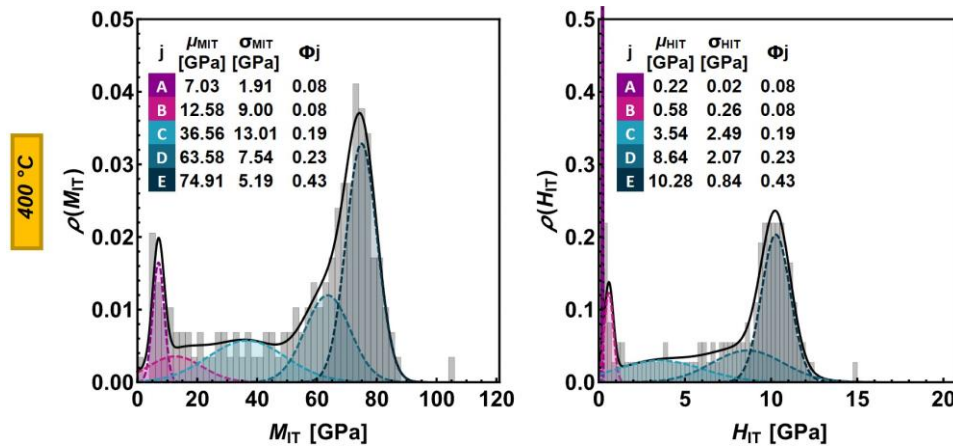


Fig. 20. Deconvoluted distributions of indentation modulus (M_{IT}) and hardness (H_{IT}) at 400°C, with Gaussian mixture components (A to E) identified

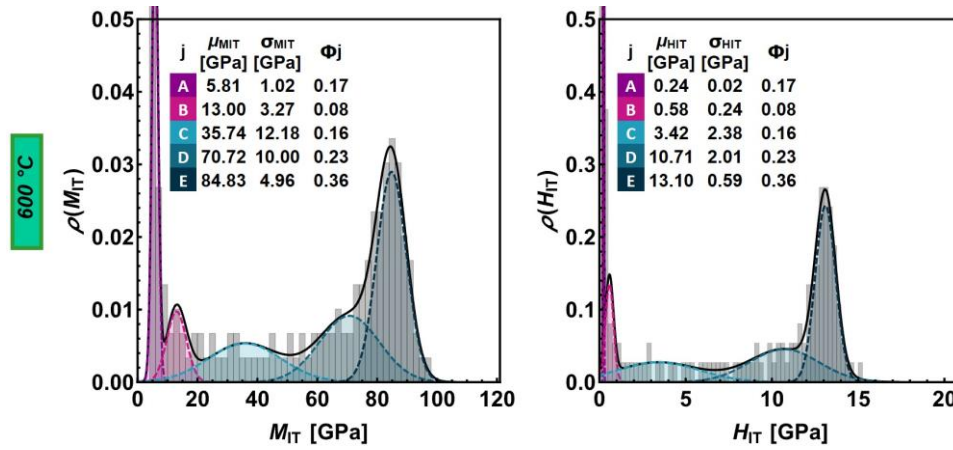


Fig. 21. Deconvoluted distributions of indentation modulus (M_{IT}) and hardness (H_{IT}) at 600°C, with Gaussian mixture components (A to E) identified

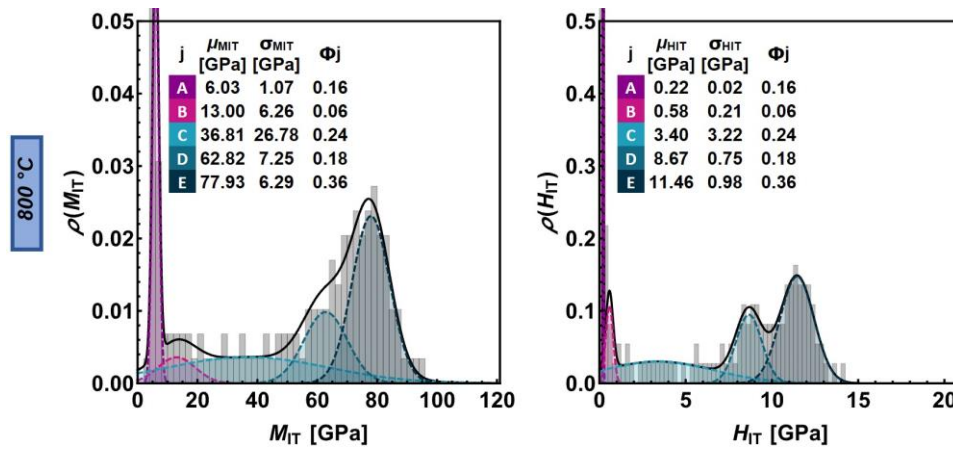


Fig. 22. Deconvoluted distributions of indentation modulus (M_{IT}) and hardness (H_{IT}) at 800°C, with Gaussian mixture components (A to E) identified

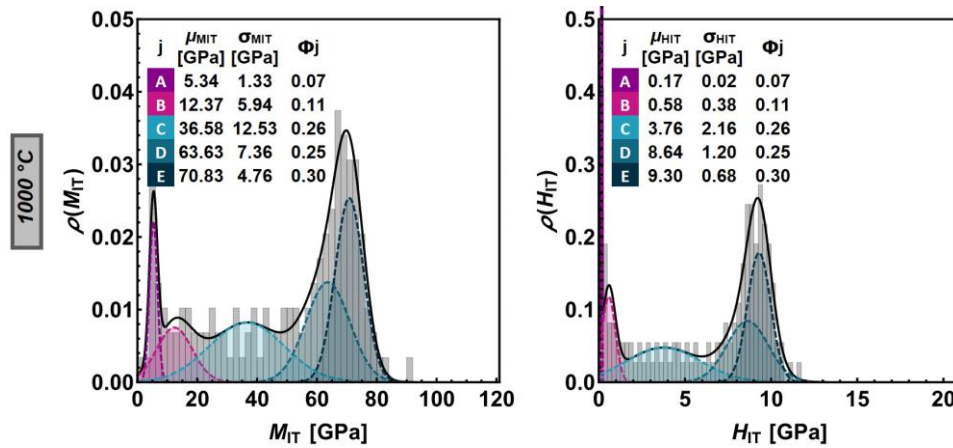


Fig. 23. Deconvoluted distributions of indentation modulus (M_{IT}) and hardness (H_{IT}) at 1000°C, with Gaussian mixture components (A to E) identified

Components D and E, representing quartz and feldspar grains, are the primary contributors to the mechanical properties of the sandstone, as they exhibit the highest mechanical parameters and volume fractions [62]. At low temperatures (up to 200°C), both M_{IT} and H_{IT} increase slightly for these components, indicating potential microstructural consolidation or thermal tightening. At 600°C, peaks in modulus and hardness are observed for components D and E, with the modulus peak being more prominent than that of the overall composite (Fig. 24). This suggests a strengthening effect attributed to thermal expansion and reduced porosity. However, above 800°C, a marked decline in M_{IT} and H_{IT} for these components reflects microstructural degradation, such as microcrack formation, grain boundary weakening, or quartz phase transformations.

Component C, representing the cementing material, displays relatively stable modulus values (30–35 GPa) and low hardness values (2–4 GPa) across all temperatures. Its stability ensures the structural cohesion of the composite, even as components D and E undergo thermal variations. Components A and B, associated with epoxy resin filling the pore space and the interface between pores and the sandstone skeleton, exhibit low mechanical properties and are not major contributors to the overall response.

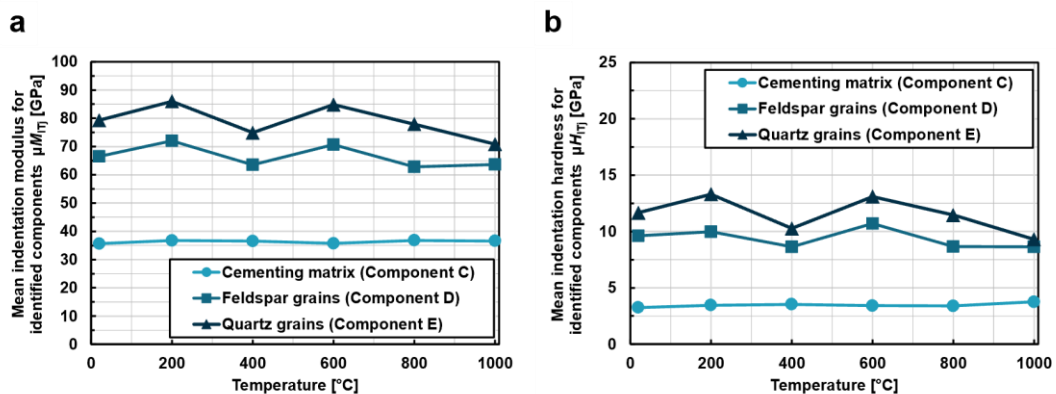


Fig. 24. Variation of the mean indentation modulus (M_{IT}) (a) and mean hardness (H_{IT}) (b) for identified components C, D and E as a function of temperature

The detailed phase-specific analysis enhances the understanding of how individual components contribute to the composite behaviour of the sandstone. The overall mechanical properties are dominated by components D and E due to their high modulus and hardness values. The observed drop in overall parameters at high temperatures is primarily attributed to the degradation of the skeleton (components D and E), rather than the cementing material (component C). Specifically, the decline in M_{IT} and H_{IT} at elevated temperatures is linked to microcrack formation, grain boundary weakening, and phase transformations in quartz, underscoring the critical role of the rock skeleton in determining the thermal response of the sandstone.

3.3. Linking the evolution of mechanical parameters to geometric changes in sandstone microstructure

Thermal treatment induces significant microstructural changes in sandstone, affecting both the pore space and the solid matrix. These geometric changes—such as variations in porosity, pore size distribution, and grain morphology—directly influence the mechanical properties of the material. By integrating micro-CT imaging with nanoindentation tests, this study provides a detailed analysis of the relationship between mechanical parameters, such as hardness (H_{IT}) and indentation modulus (M_{IT}), and

morphological transformations. This section examines the interplay between these factors by correlating mechanical responses at different temperature thresholds with geometric changes identified through micro-CT analysis.

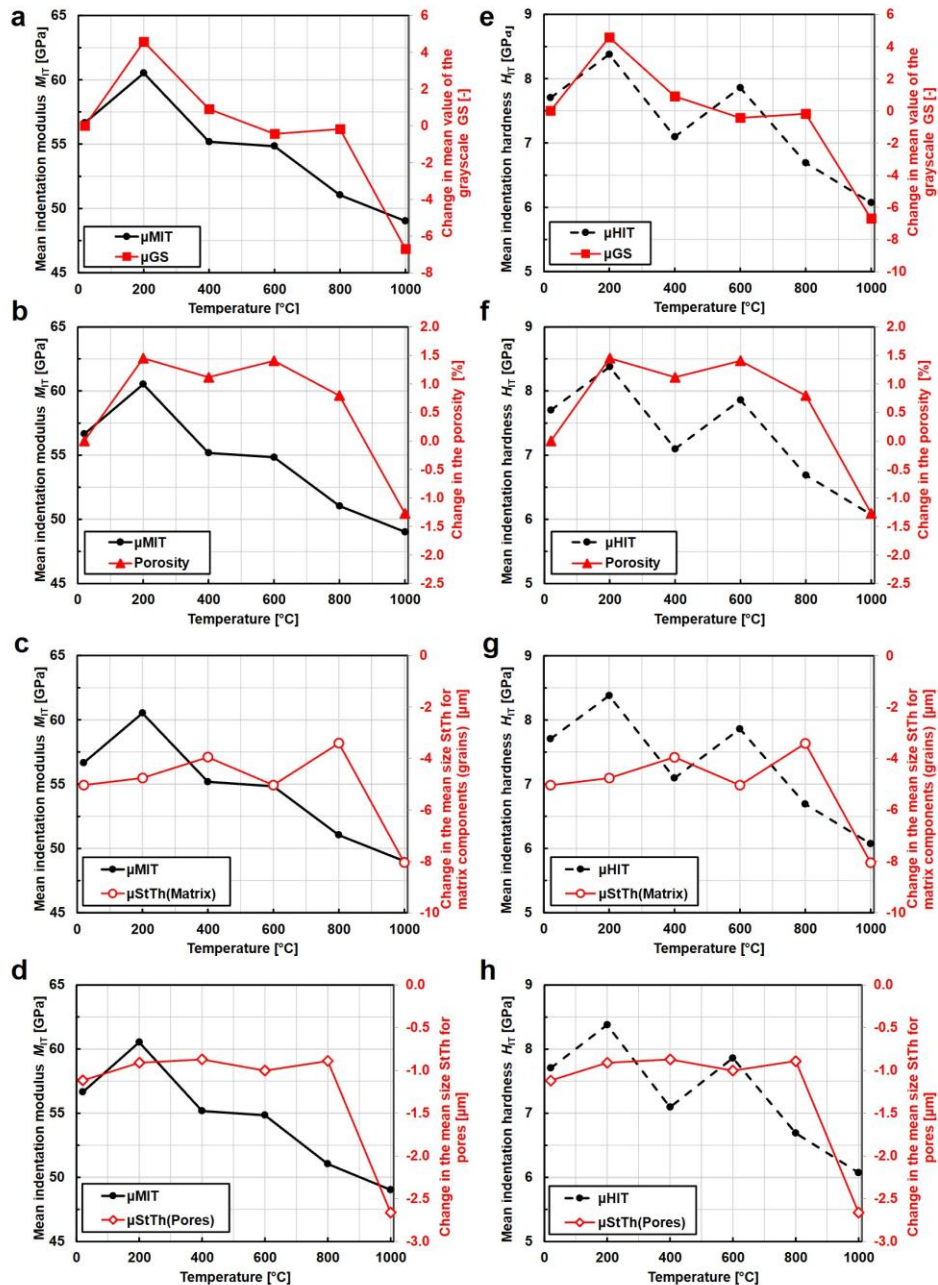


Fig. 25. Variation of mean indentation modulus (M_{IT}) and mean hardness (H_{IT}) as a function of temperature, compared to changes in microstructural parameters: (a, e) mean grayscale value (μGS), (b, f) porosity, (c, g) mean structure thickness of the matrix $\mu StTh(Matrix)$, and (d, h) mean structure thickness of the pores $\mu StTh(Pores)$

Microstructural changes were quantified as the difference between a given measure's value before and after thermal treatment at a specific temperature. A negative change indicates an increase in the corresponding microstructural feature (e.g., porosity or other geometric parameters) relative to the reference sample. Among the analyzed geometric measures, all show a strong correlation with the mechanical properties and microstructural evolution of the sandstone. In the higher temperature range (above a specific threshold), a decrease in the relative values of key geometric measures aligns with a reduction in the material's mechanical properties.

The results confirm that mechanical parameters are significantly influenced by changes in the pore space. An increase in porosity and pore sizes, particularly at higher temperatures, leads to reductions in both M_{IT} and H_{IT} . This is attributed to the increased presence of microcracks and a decline in microstructural cohesion. Pore space plays a critical role in weakening the structure by altering local stress concentrations and affecting the material's effective absorption of radiation, as reflected in changes to the absorption coefficient (grayscale values).

The distribution of the reconstructed absorption coefficient shows a strong alignment with trends in mechanical parameter variations. While a similar correlation exists for hardness, the agreement between grayscale values and mechanical parameters is stronger for M_{IT} . This suggests that changes in grayscale values can reliably estimate mechanical parameter variations, provided baseline mechanical parameters are known for at least one temperature threshold.

The evolution of mechanical parameters results from a complex combination of geometric changes in the microstructure (e.g., increased porosity and altered structure thickness in both the skeleton and pore space) and changes in the mechanical properties of individual sandstone components.

Notably, components D and E (quartz and feldspar grains) exhibit significant evolution in their mechanical properties with increasing temperature, directly impacting the mean mechanical parameters of the material. In contrast, component C (cementing material) remains relatively stable across the temperature range. However, its lower mechanical contribution limits its ability to compensate for the degradation of components D and E, which dominate the mechanical response of the sandstone.

4. CONCLUSIONS

This study investigated the thermal evolution of siliceous sandstone microstructure and mechanical properties using a combination of microcomputed tomography (micro-CT) and nanoindentation techniques. The material, quarried in the Kielce Upland, was subjected to temperatures ranging from 20°C to 1000°C. The findings provide key insights into the relationship between geometric changes and mechanical parameter variations across this temperature range, focusing on fine-grained siliceous sandstones. The most striking conclusions are as follows:

- i. Geometric changes in the microstructure, including porosity, pore size distribution, and structural thickness of the solid matrix, strongly correlate with variations in mechanical parameters. At higher temperatures, increased porosity and reduced structural thickness correspond to a significant decline in indentation modulus (M_{IT}) and hardness (H_{IT}), indicating microstructural degradation.
- ii. At moderate temperatures (20–200°C), temporary strengthening of the sandstone is observed, with increases in M_{IT} and H_{IT} , attributed to microstructural compaction and reduced pore space.
- iii. At higher temperatures (>600°C), declines in both mechanical and geometric parameters are primarily due to microcrack formation, increased porosity, and degradation of the sandstone matrix.
- iv. Components D and E (quartz and feldspar grains) dominate the mechanical response of the sandstone due to their higher modulus and hardness. Component C (cementing material)

remains stable but contributes less to overall strength due to its lower mechanical parameters, providing cohesion particularly at lower temperatures.

- v. Changes in grayscale values (reconstructed attenuation coefficients) are strongly correlated with M_{IT} and can reliably predict variations in mechanical properties if baseline parameters are known. Additional geometric measures, such as porosity and structural thickness, further explain the mechanisms driving sandstone behaviour under thermal stress.

Presented results should be validated against macroscopic-scale mechanical tests to better understand how microstructural changes translate to engineering-scale performance. Additionally, detailed petrographic analyses are recommended to precisely determine the mineral composition of the sandstone and assess potential changes in mineralogy during thermal treatment. At the same time ongoing studies on other sandstone types from the Kielce Upland aim to explore correlations between microstructural measures and thermal responses. Comparative analyses will help establish broader patterns and refine the understanding of sandstone behavior under thermal treatment.

REFERENCES

1. Ma, X, Dong, W, Hu, D and Zhou, H 2023. Mechanical properties of granite at high temperature subjected to true triaxial compression. *International Journal of Rock Mechanics and Mining Sciences* **164**, 105313.
2. Li, Y, Zhai, Y, Xie, Y and Meng, F 2023. Research on the Impact Mechanical Properties of Real-Time High-Temperature Granite and a Coupled Thermal–Mechanical Constitutive Model. *Materials* **16**, 2773.
3. Hou, B, Sun, F, Xue, S and Zhang, X 2022. Experimental study on mechanical properties and porosity and permeability of rock in high temperature environment. *Journal of Physics: Conference Series* **2368**, 012031.
4. Dean, SW, Takarli, M and Prince-Agbodjan, W 2008. Temperature Effects on Physical Properties and Mechanical Behavior of Granite: Experimental Investigation of Material Damage. *Journal of ASTM International* **5**, 100464.
5. PG, R, Viète, DR, Chen, BJ and Perera, MSA 2012. Transformation plasticity and the effect of temperature on the mechanical behaviour of Hawkesbury sandstone at atmospheric pressure. *Engineering Geology* **151**, 120–127.
6. Sygala, A, Bukowska, M and Janoszek, T 2013. High Temperature Versus Geomechanical Parameters of Selected Rocks – The Present State of Research. *Journal of Sustainable Mining* **12**, 45–51.
7. Tian, H, Kempka, T, Yu, S and Ziegler, M 2016. Mechanical Properties of Sandstones Exposed to High Temperature. *Rock Mechanics and Rock Engineering* **49**, 321–327.
8. Yasuhara, H, Kinoshita, N, Ohfuji, H, Takahashi, M, Ito, K and Kishida, K 2015. Long-term observation of permeability in sedimentary rocks under high-temperature and stress conditions and its interpretation mediated by microstructural investigations. *Water Resources Research* **51**, 5425–5449.
9. Lintao, Y, Marshall, AM, Wanatowski, D, Stace, R and Ekneligoda, T 2017. Effect of high temperatures on sandstone – a computed tomography scan study. *International Journal of Physical Modelling in Geotechnics* **17**, 75–90.
10. Lei, R, Wang, Y, Zhang, L, Liu, B, Long, K, Luo, P and Wang, Y 2019. The evolution of sandstone microstructure and mechanical properties with thermal damage. *Energy Science & Engineering* **7**, 3058–3075.

11. Cheng, C and Milsch, H 2020. Permeability Variations in Illite-Bearing Sandstone: Effects of Temperature and NaCl Fluid Salinity. *Journal of Geophysical Research: Solid Earth* **125**.
12. Zheng, Y, Zhang, L, Wu, P, Guo, X, Li, M and Zhu, F 2024. Physical and Mechanical Properties and Damage Mechanism of Sandstone at High Temperatures. *Applied Sciences* **2024**.
13. Fan, LF, Gao, JW, Wu, ZJ, Yang, SQ and Ma, GW 2018. An investigation of thermal effects on micro-properties of granite by X-ray CT technique. *Applied Thermal Engineering* **140**, 505–519.
14. Shen, Y-J, Zhang, Y-L, Gao, F, Yang, G-S and Lai, X-P 2018. Influence of Temperature on the Microstructure Deterioration of Sandstone. *Energies* **11**, 1753.
15. Li, J, Du, Z-W and Guo, Z-P 2020. Effect of High Temperature (600°C) on Mechanical Properties, Mineral Composition, and Microfracture Characteristics of Sandstone. *Advances in Materials Science and Engineering* **2020**.
16. Róžański, A, Róžańska, A, Sobótka, M, Pachnicz, M and Bukowska, M 2021. Identification of changes in mechanical properties of sandstone subjected to high temperature: meso- and micro-scale testing and analysis. *Archives of Civil and Mechanical Engineering* **21**, 28.
17. Elliott, JC and Dover, SD 1982. X-ray microtomography. *Journal of Microscopy* **126**, 211–213.
18. Stock, SR 1999. X-ray microtomography of materials. *International Materials Reviews* **44**, 141–164.
19. Maire, E, Buffière, JY, Salvo, L, Blandin, JJ, Ludwig, W and Létang, JM 2001. On the Application of X-ray Microtomography in the Field of Materials Science. *Advanced Engineering Materials* **B**, 539.
20. Stock, SR 2008. Recent advances in X-ray microtomography applied to materials. *International Materials Reviews* **53**, 129–181.
21. Landis, EN and Keane, DT 2010. X-ray microtomography. *Materials characterization* **61**, 1305–1316.
22. Fischer-Cripps, AC and Nicholson, DW 2004. Nanoindentation. Mechanical engineering series. *Appl. Mech. Rev* **57**, B12–B12.
23. Schuh, CA 2006. Nanoindentation studies of materials. *Materials today* **9**, 32–40.
24. Mukhopadhyay, NK and Paufler, P 2006. Micro- and nanoindentation techniques for mechanical characterisation of materials. *International Materials Reviews* **51**, 209–245.
25. Oyen, ML and Cook, RF 2009. A practical guide for analysis of nanoindentation data. *Journal of the mechanical behavior of biomedical materials* **2**, 396–407.
26. Lucca, DA, Herrmann, K and Klopstein, MJ 2010. Nanoindentation: Measuring methods and applications. *CIRP annals* **59**, 803–819.
27. Appoloni, CR, Fernandes, CP and Rodrigues, CRO 2007. X-ray microtomography study of a sandstone reservoir rock. *Nuclear Instruments and Methods in Physics Research Section A: Accelerators, Spectrometers, Detectors and Associated Equipment* **580**, 629–632.
28. Zhu, W, Hughes, JJ, Bicanic, N and Pearce, CJ 2007. Nanoindentation mapping of mechanical properties of cement paste and natural rocks. *Materials characterization* **58**, 1189–1198.
29. Zandomenighi, D, Voltolini, M, Mancini, L, Brun, F, Dreossi, D and Polacci, M 2010. Quantitative analysis of X-ray microtomography images of geomaterials: Application to volcanic rocks. *Geosphere* **6**, 793–804.
30. Baker, DR, Mancini, L, Polacci, M, Higgins, MD, Gualda, GAR, Hill, RJ and Rivers, ML 2012. An introduction to the application of X-ray microtomography to the three-dimensional study of igneous rocks. *Lithos* **148**, 262–276.
31. Bielecki, J, Jarzyna, J, Bożek, S, Lekki, J, Stachura, Z and Kwiatek, WM 2013. Computed microtomography and numerical study of porous rock samples. *Radiation Physics and Chemistry* **93**, 59–66.

32. Shukla, P, Taneja, S, Sondergeld, C and Rai, C 2015. Nanoindentation Measurements on Rocks. Fracture, Fatigue, Failure, and Damage Evolution, Volume 5. J. Carroll and S. Daly, eds. Springer International Publishing, 99–105.
33. Ma, Z, Pathegama Gamage, R and Zhang, C 2020. Application of nanoindentation technology in rocks: a review. *Geomechanics and Geophysics for Geo-Energy and Geo-Resources* **6**, 60.
34. Górska-Zabielska, M 2021. The Rock Garden of the Institute of Geography and Environmental Sciences, Jan Kochanowski University—A New Geo-Site in Kielce, Central Poland. *Geosciences* **11**.
35. Folk, RL 1954. The Distinction between Grain Size and Mineral Composition in Sedimentary-Rock Nomenclature. *The Journal of Geology* **62**, 344–359.
36. Lambert, JH 1760. I. H. Lambert ... Photometria sive de mensura et gradibus luminis, colorum et umbrae [Photometry or the measurement and degrees of light, colors and shade]. Augustae Vindelicorum : sumptibus viduae Eberhardi Klett typis Chistophori Petri Detleffsen.
37. Beer 1852. Bestimmung der Absorption des rothen Lichts in farbigen Flüssigkeiten [Determination of the absorption of red light in colored liquids]. *Annalen der Physik*. **162**, 78–88.
38. Ingle, DJ 1988. Crouch. SR Spectrochemical Analysis Prentice Hall.
39. Otsu, N 1979. A Threshold Selection Method from Gray-Level Histograms. *IEEE Transactions on Systems, Man, and Cybernetics* **9**, 62–66.
40. Bruker-MicroCT CT-Analyser: morphometric parameters in 3D and 2D. Bruker.
41. Constantinides, G, Chandran, K.R, Ulm, F.-J and Van Vliet, K.J 2006. Grid indentation analysis of composite microstructure and mechanics: Principles and validation. *Materials Science and Engineering: A* **430**, 189–202.
42. Hoan, PT and Thuong, NT 2021. Microstructural characteristics of ultra-high performance concrete by grid nanoindentation and statistical analysis. *Journal of Science and Technology in Civil Engineering (STCE) - NUCE* **15**, 90–101.
43. Anton Paar 2023. Quick matrix mode for grid indentation method. Anton Paar.
44. Doerner, MF and Nix, WD 1986. A method for interpreting the data from depth-sensing indentation instruments. *Journal of Materials Research* **1**, 601–609.
45. Oliver, WC and Pharr, GM 2004. Measurement of hardness and elastic modulus by instrumented indentation: Advances in understanding and refinements to methodology. *Journal of materials research* **19**, 3–20.
46. Oliver, WC and Pharr, GM 1992. An improved technique for determining hardness and elastic modulus using load and displacement sensing indentation experiments. *Journal of Materials Research* **7**, 1564–1583.
47. Velez, K, Maximilien, S, Damidot, D, Fantozzi, G and Sorrentino, F 2001. Determination by nanoindentation of elastic modulus and hardness of pure constituents of Portland cement clinker. *Cement and Concrete Research* **31**, 555–561.
48. Wang, H, Lin, H, Cao, P 2017. Correlation of UCS Rating with Schmidt Hammer Surface Hardness for Rock Mass Classification. *Rock Mech Rock Eng* **50**, 195–203.
49. Chau, KT, Wong RHC 1996. Uniaxial compressive strength and point load strength of rocks. *International Journal of Rock Mechanics and Mining Sciences & Geomechanics Abstracts* **33**, 183–188.
50. Dinçer, İ, Acar, A, Çobanoğlu, I, et al 2004. Correlation between Schmidt hardness, uniaxial compressive strength and Young's modulus for andesites, basalts and tuffs. *Bulletin of Engineering Geology and the Environment* **63**, 141–148.
51. Basu, A, Mishra, D, Roychowdhury, K 2013. Rock failure modes under uniaxial compression, Brazilian, and point load tests. *Bulletin of Engineering Geology and the Environment* **72**.

52. Cala, M, Cyran, K, Kawa, M, Kolano, M, Lydzba, D, Pachnicz, M, Rajczakowska, M, Rózanski, A, Sobótka, M, Stefaniuk, D, Stopkowicz, A and Walach, D 2017. *Identification of Microstructural Properties of Shale by combined Use of X-Ray Micro-CT and Nanoindentation Tests*. ISRM European Rock Mechanics Symposium - EUROCK 2017, Ostrava, Czech Republic, June 2017
53. Gorzelańczyk, T, Pachnicz, M, Róžański, A and Schabowicz, K 2019. Multi-Scale Structural Assessment of Cellulose Fibres Cement Boards Subjected to High Temperature Treatment. *Materials* **12**, 2449.
54. Gorzelańczyk, T, Pachnicz, M, Róžański, A and Schabowicz, K 2020. Identification of microstructural anisotropy of cellulose cement boards by means of nanoindentation. *Construction and Building Materials* **257**, 119515.
55. Wolfram Research, Inc Mathematica, Version 12.0.
56. Van Rossum, G and Drake Jr, FL 1995. Python reference manual. Centrum voor Wiskunde en Informatica Amsterdam.
57. Pedregosa, F et al. 2011. Scikit-learn: Machine Learning in Python. *Journal of Machine Learning Research*. **12**, 2825–2830.
58. Eidelman, A 2020. Python Data Science Handbook by Jake VANDERPLAS (2016). *Statistique et Société*. **8**, 45–47.
59. Li, M and Liu, X 2022. Effect of Thermal Treatment on the Physical and Mechanical Properties of Sandstone: Insights from Experiments and Simulations. *Rock Mechanics and Rock Engineering* **55**, 3171–3194.
60. Schwarz, G 1978. Estimating the dimension of a model. *The annals of statistics*, 461–464.
61. Akaike, H 1998. Information theory and an extension of the maximum likelihood principle. *Selected papers of Hirotugu Akaike*. 199–213.
62. He, C, Mishra, B, Shi, Q, Zhao, Y, Lin, D and Wang, X 2023. Correlations between mineral composition and mechanical properties of granite using digital image processing and discrete element method. *International Journal of Mining Science and Technology* **33**, 949–962.